

DUVET: Spatially Resolved Observations of Star Formation Regulation via Galactic Outflows in a Starbursting Disk Galaxy

Bronwyn Reichardt Chu^{1,2} , Deanne B. Fisher^{1,2} , Alberto D. Bolatto³ , John Chisholm⁴ , Drummond Fielding⁵ , Danielle Berg⁴ , Alex J. Cameron⁶ , Karl Glazebrook^{1,2} , Rodrigo Herrera-Camus⁷ , Glenn G. Kacprzak^{1,2} , Laura Lenkic⁸ , Miao Li⁹, Daniel K. McPherson^{1,2} , Nikole M. Nielsen^{1,2} , Danail Obreschkow¹⁰ , Ryan J. Rickards Vaught¹¹ , and Karin Sandstrom¹¹

¹ Centre for Astrophysics and Supercomputing, Swinburne University of Technology, Hawthorn, VIC 3122, Australia

² ARC Centre of Excellence for All Sky Astrophysics in 3 Dimensions (ASTRO 3D), Australia

³ Department of Astronomy, University of Maryland, College Park, MD 20742, USA

⁴ Department of Astronomy, University of Texas, Austin, TX 78712, USA

⁵ Center for Computational Astrophysics, Flatiron Institute, 162 Fifth Avenue, New York, NY 10010, USA

⁶ Department of Physics, University of Oxford, Denys Wilkinson Building, Keble Road, Oxford, OX1 4RH, UK

⁷ Departamento de Astronomía, Universidad de Concepción, Barrio Universitario, Concepción, Chile

⁸ SOFIA Science Center, USRA, NASA Ames Research Center, M.S. N232-12, Moffett Field, CA 94035, USA

⁹ Department of Physics, Zhejiang University, 866 Yuhangtang Road, Hangzhou, 310058, People's Republic of China

¹⁰ International Centre for Radio Astronomy Research (ICRAR), M468, University of Western Australia, 35 Stirling Highway, Crawley, WA 6009, Australia

¹¹ Center for Astrophysics and Space Sciences, Department of Physics, University of California, San Diego, CA, USA

Received 2022 August 9; revised 2022 November 2; accepted 2022 November 8; published 2022 December 20

Abstract

We compare 500 pc scale, resolved observations of ionized and molecular gas for the $z \sim 0.02$ starbursting disk galaxy IRAS08339+6517, using measurements from KCWI and NOEMA. We explore the relationship of the star-formation-driven ionized gas outflows with colocated galaxy properties. We find a roughly linear relationship between the outflow mass flux ($\dot{\Sigma}_{\text{out}}$) and star formation rate surface density (Σ_{SFR}), $\dot{\Sigma}_{\text{out}} \propto \Sigma_{\text{SFR}}^{1.06 \pm 0.10}$, and a strong correlation between $\dot{\Sigma}_{\text{out}}$ and the gas depletion time, such that $\dot{\Sigma}_{\text{out}} \propto t_{\text{dep}}^{-1.1 \pm 0.06}$. Moreover, we find these outflows are so-called *breakout* outflows, according to the relationship between the gas fraction and disk kinematics. Assuming that ionized outflow mass scales with total outflow mass, our observations suggest that the regions of highest Σ_{SFR} in IRAS08 are removing more gas via the outflow than through the conversion of gas into stars. Our results are consistent with a picture in which the outflow limits the ability of a region of a disk to maintain short depletion times. Our results underline the need for resolved observations of outflows in more galaxies.

Unified Astronomy Thesaurus concepts: Galaxy winds (626); Galaxy evolution (594); Starburst galaxies (1570); Galaxies (573)

1. Introduction

Galactic outflows are observed ubiquitously in star-forming galaxies across cosmic time (Heckman et al. 2000; Chen et al. 2010; Steidel et al. 2010; Newman et al. 2012; Arribas et al. 2014; Rubin et al. 2014; Rodríguez del Pino et al. 2019; Veilleux et al. 2020; Bolatto et al. 2021) and play a critical role in galaxy evolution models (e.g., Somerville & Davé 2015). When star-formation-driven outflows are not included, models are unable to reproduce basic galaxy properties such as the galaxy mass function, galaxy sizes, and the Kennicutt–Schmidt law (see review by Somerville & Davé 2015). The most energetic winds are observed coming from active galactic nuclei (Veilleux et al. 2005; Fluetsch et al. 2019; Förster Schreiber et al. 2019), which send gas into the halo (Nelson et al. 2019; Oppenheimer et al. 2020). Galactic fountains arising from clusters of intense star formation remove gas from their local region (e.g., Bolatto et al. 2013a; Leroy et al. 2015a; Salak et al. 2020), which is then recycled into the disk after moving through the lower regions of the halo.

Star-formation-driven outflows are widely thought to play multiple roles in regulating star formation. One such role is to

directly remove gas from regions of active star formation, for example, as observed in nearby starbursts NGC 253 (Bolatto et al. 2013a) and M82 (Leroy et al. 2015b). In such environments, the mass-loss rate due to the wind can be comparable to the rate at which gas is converted into stars.

Moreover, theory argues that the energy and momentum injected from supernovae-driven winds play a regulatory role by increasing the turbulence of the interstellar medium (ISM; e.g. Ostriker et al. 2010; Faucher-Giguère et al. 2013; Hayward & Hopkins 2017; Krumholz et al. 2018). The increased turbulence is critical to providing pressure support in galaxies, setting the thickness of the gas disk, and preventing runaway star formation, and is known as star formation feedback. This regulation generates a local balance between the inward gravitational pressure on the disk, characterized by the molecular and stellar mass surface densities, and the outward pressure provided by the feedback, which is typically characterized by the star formation rate (SFR) surface density multiplied by an efficiency factor (for a description see Kim et al. 2013). Observations do recover positive correlations of gravitational pressure with an SFR surface density over 6 orders of magnitude (Fisher et al. 2019; Sun et al. 2020; Barrera-Ballesteros et al. 2021; Girard et al. 2021), albeit those published thus far find shallower power-law slopes than theory predicts. Ostriker & Kim (2022) argued that this may be due to systematics in the estimations of pressure. L. Lenkic et al. 2022



Original content from this work may be used under the terms of the [Creative Commons Attribution 4.0 licence](https://creativecommons.org/licenses/by/4.0/). Any further distribution of this work must maintain attribution to the author(s) and the title of the work, journal citation and DOI.

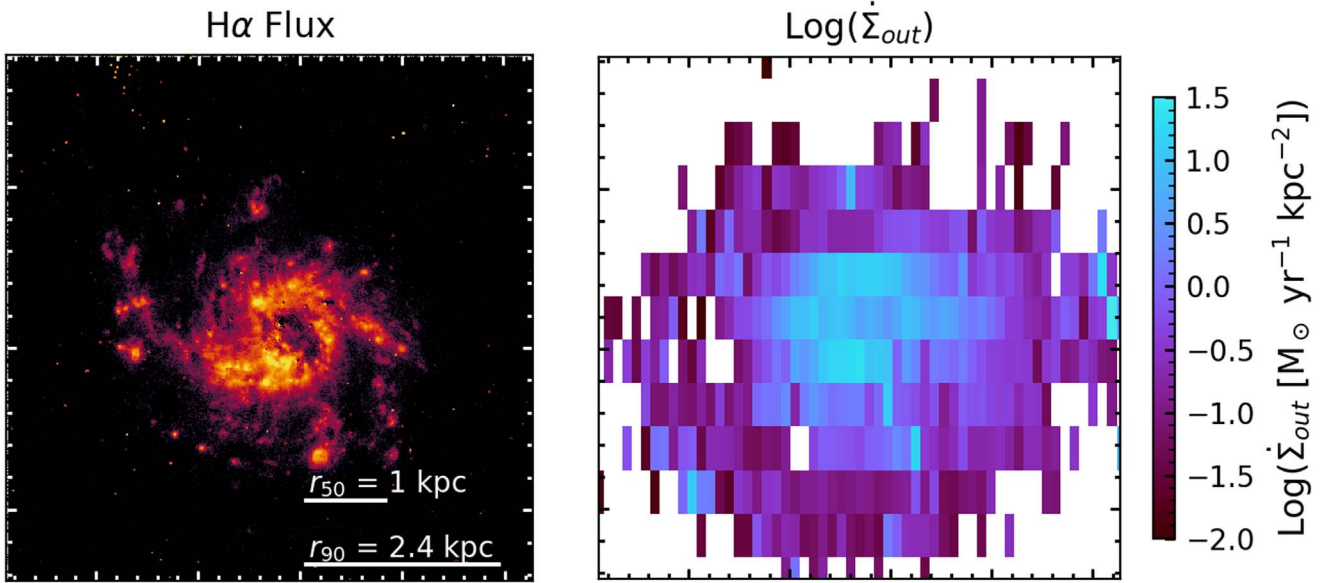


Figure 1. Maps of IRAS08. (Left) Map of H α flux from HST. (Right) Mass-outflow flux, $\dot{\Sigma}_{\text{out}}$, found in each spaxel using [O III] $\lambda 5007$ and H β emission line flux from observations with KCWI on board Keck II (RC22). Only spaxels where an outflow was detected are included. The $\dot{\Sigma}_{\text{out}}$ values were scaled to assume electron densities of $n_e = 100 \text{ cm}^{-3}$. Outflowing gas driven by star formation has been resolved across the disk of IRAS08.

in preparation will investigate this. It is not clear how outflows may impact feedback-regulated star formation theory. Theoretical work employing results from supernova clustering suggests that clustering may lead to increases in the momentum input into the ISM (Fielding et al. 2018; Gentry et al. 2020). Conversely, Orr et al. (2022a) argued that if winds leave the disk they carry momentum with them, which might reduce turbulence.

Current theory, therefore, implies that supernova-driven winds (or outflows) play multiple roles: (1) removing gas directly from disks and (2) injecting turbulence into the ISM. Resolved observations of outflows are, however, challenging due to the intrinsic faintness of the spectral features of the wind. We use data from the DUVET sample (D. B. Fisher et al. 2022 in preparation) that uses high signal-to-noise ratio (S/N) observations from the Keck Cosmic Web Imager (KCWI) to study resolved properties of outflows in rare starburst disk galaxies at $z \approx 0.01$ –0.03 (e.g., Cameron et al. 2021; Reichardt Chu et al. 2022). In this paper, we focus on using resolved outflow observations of IRAS 08339+6517 from the DUVET sample to compare the properties of molecular gas and star formation.

The paper is organized as follows. We describe our target galaxy, IRAS 08339+6517 (hereafter IRAS08), in Section 2.1. Our observations and data reduction of IRAS08 for ionized gas are described in Section 2.2, and for molecular gas in Section 2.3, together with our methods. In Section 2.4, we find resolved stellar masses for IRAS08. In Sections 3.1–3.3, we explore the relationship between outflows and the SFR surface density and the molecular gas surface density. In Sections 3.4 and 3.5, we compare our resolved outflow observations to models. A summary of our results and conclusions is presented in Section 4. We assume a flat Lambda cold dark matter cosmology with $H_0 = 69.3 \text{ km Mpc}^{-1} \text{ s}^{-1}$ and $\Omega_0 = 0.3$ (Hinshaw et al. 2013).

2. Observations and Methods

Our analysis combines observations of outflows from Reichardt Chu et al. (2022; hereafter RC22) with observations of molecular gas from Fisher et al. (2022; hereafter F22). All data have been published, and the data reduction methods are described in more detail in those papers. We briefly summarize these data and methods here.

2.1. IRAS 08339+6517

IRAS08 is a face-on, UV-bright, blue-compact galaxy at $z \approx 0.0191$. It is a $10 \times$ outlier from the $z = 0$ star-forming main sequence. In Figure 1 we show the H α flux map from the Hubble Space Telescope (HST), which shows IRAS08’s star-forming ring. IRAS08’s young stellar population has been shown to be consistent with containing super-star clusters in HST/COS spectra (Otí-Floranes et al. 2014). For more physical properties of IRAS08, see Table 1.

IRAS08 is well known to host a strong outflow (Leitherer et al. 2013; Chisholm et al. 2015; Reichardt Chu et al. 2022). The benefit of studying IRAS08 is that since it is mostly face-on, we can make point-to-point comparisons between the outflow properties and the molecular gas.

2.2. KCWI Observations of SFR and Outflows

IRAS08 was observed with KCWI (Morrissey et al. 2018) using the BM grating in the large slicer mode (field of view: $33.'' \times 20.4''$) for 20 minutes with the central wavelength setting at $\lambda = 4800\text{\AA}$. These observations are described in both RC22 and F22. The data were reduced using the standard IDL pipeline (version 1.1.0) and in-frame sky subtraction. A continuum fit and subtraction was applied using pPXF (Cappellari 2017) with BPASS templates (version 2.2.1; Stanway & Eldridge 2018).

To measure SFR and outflow properties we follow a very similar procedure as described in RC22. The most significant

Table 1
Galaxy Properties of IRAS 08339+6517

| Property | | Value | Reference |
|--|--|--------------------------------------|-------------------------|
| Redshift | z | 0.0191 | Kim et al. (1995) |
| Inclination | i | 13° | Leitherer et al. (2013) |
| Stellar mass | M_* | $1.1 \pm 0.3 \times 10^{10} M_\odot$ | F22 |
| Star formation rate | SFR | $12.1 \pm 1 M_\odot \text{ yr}^{-1}$ | F22 |
| Stellar population age | | 10 Myr | Leitherer et al. (2002) |
| Molecular gas fraction | f_{gas} | 17% | F22 |
| Toomre stability parameter | Q_{gas} | 0.5 | F22 |
| Resolved ionized gas mass-outflow rate ($n_e = 100 \text{ cm}^{-3}$) | \dot{M}_{out} | $34.7 M_\odot \text{ yr}^{-1}$ | RC22 |
| Resolved ionized gas mass-outflow rate ($n_e = 300 \text{ cm}^{-3}$) | \dot{M}_{out} | $11.6 M_\odot \text{ yr}^{-1}$ | RC22 |
| Total galaxy ionized gas mass-loading factor (from absorption) | $\dot{M}_{\text{out}}/\text{SFR}_{\text{cos}}$ | 0.07 | Chisholm et al. (2017) |
| Resolved ionized gas mass-loading factor ($n_e = 100 \text{ cm}^{-3}$) | η | 3.2 | RC22 |

Note. The mass-loading factor η from RC22 is calculated using the SFR from only those regions of the galaxy where outflows are observed.

adjustment is that we modify the adopted electron density (discussed below).

KCWI spaxels are non-square, with dimensions of $0.^{\circ}29 \times 1.^{\circ}36$ for the large slicer. RC22 carried out an analysis in which outflows were fit in various spatial bin sizes. They found that correlations of outflow physical properties are more stable for bin sizes of 5×1 spatial sampling of the KCWI data and larger, summing the spectra in each set of 5×1 spaxels. In order to more easily interpret the data, we resample all data sets to match this 5×1 spatial sampling of the KCWI data. This binning corresponds to sizes of $1.^{\circ}46 \times 1.^{\circ}36$, which in physical scale is $0.57 \times 0.53 \text{ kpc}$.

Following the method described in RC22, to identify outflows we fit both a single and a double Gaussian profile to the H β emission lines in spaxels where the continuum has an S/N greater than 10 pixel^{-1} . We used the Bayesian information criterion to decide whether the extra parameters in the double Gaussian fit are required. When two Gaussians are required, we assume that the broad second Gaussian represents the outflowing gas (see RC22 for more detail).

Using the double Gaussian fits, we calculated the outflow velocity

$$v_{\text{out}} = |v_{\text{narrow}} - v_{\text{broad}}| + 2\sigma_{\text{broad}}, \quad (1)$$

where v_{narrow} and v_{broad} are the velocities at the center of the narrow and broad Gaussians, respectively, and σ_{broad} is the standard deviation of the broad Gaussian. This definition of v_{out} is comparable to the velocity at 90% of the continuum, v_{90} , measured from absorption line studies (e.g., Rupke et al. 2005; Chisholm et al. 2015, 2016), and similar to previous emission line studies (e.g., Genzel et al. 2011; Davies et al. 2019; Fluetsch et al. 2019).

The mass-outflow rate is defined as

$$\dot{M}_{\text{out}} = \frac{1.36 m_{\text{H}}}{\gamma_{\text{H}\beta} n_e} \left(\frac{v_{\text{out}}}{R_{\text{out}}} \right) L_{\text{H}\beta, \text{broad}}, \quad (2)$$

where m_{H} is the atomic mass of hydrogen, $\gamma_{\text{H}\beta}$ is the H β emissivity at electron temperature $T_e = 10^4 \text{ K}$ for case B recombination ($\gamma_{\text{H}\beta} = 1.24 \times 10^{-25} \text{ erg cm}^3 \text{ s}^{-1}$; Osterbrock & Ferland 2006), n_e is the local electron density in the outflow, R_{out} is the radial extent of the outflow, and $L_{\text{H}\beta, \text{broad}}$ is the extinction-corrected H β luminosity of the broad component. We assume $R_{\text{out}} = 0.5 \text{ kpc}$; see the discussion in RC22 for the motivation and the likely systematic uncertainty on R_{out} .

RC22 showed that the main driver of \dot{M}_{out} is the luminosity of the broad component, with only a small dependence on the outflow velocity. In IRAS08, there is an ~ 2 order-of-magnitude variation in the broad-component luminosity, but only a factor of a few change in velocity.

There is an explicit inverse dependence of \dot{M}_{out} on $\gamma_{\text{H}\beta}$. Since $\gamma_{\text{H}\beta}$ depends inversely on T_e , different assumptions in T_e directly change the derived \dot{M}_{out} . Cameron et al. (2021) provide a direct measurement of T_e from the [O III] $\lambda 4363$ line for MRK 1486. They found that T_e decreases in the outflow compared to the disk by an order of $\sim 1000 \text{ K}$, with a typical outflow T_e of $\sim 12,000\text{--}14,000 \text{ K}$. IRAS08 has a higher metallicity than MRK 1486, ($0.7 Z_\odot$; López-Sánchez et al. 2006), which corresponds to a lower T_e (Kewley et al. 2019). Indeed, López-Sánchez et al. (2006) derive $T_e \sim 8000 \text{ K}$ for IRAS08. There is no evidence that the metallicity varies across the disk of IRAS08 (López-Sánchez et al. 2006; Fisher et al. 2022). We, therefore, assume a constant T_e throughout our outflow. Using the code PyNeb (Luridiana et al. 2015), we find that if we assume an electron temperature for the outflow of $T_e = 7000 \text{ K}$, the derived \dot{M}_{out} would be $1.4 \times$ higher than we find for our standard assumption of $T_e = 10^4 \text{ K}$. Conversely, if we assume a high electron temperature of $T_e = 14,000 \text{ K}$, the \dot{M}_{out} would be $0.7 \times$ lower.

We do not know a priori what electron density n_e should be adopted for the outflows. We only have access to the [O II] density tracer, but the broad outflow components are blended in the spectrum such that we do not have sufficient spectral resolution to measure the electron density of the outflow in IRAS08. We therefore must adopt a value. The electron density of IRAS08 based on the total integrated [O II] emission line ratio from the galaxy and outflow, together, is of order $\sim 300\text{--}400 \text{ cm}^{-3}$. Standard assumptions expect n_e to decline in the outflow compared to the disk, though recent work suggests this may not be the case (Förster Schreiber et al. 2019; Fluetsch et al. 2021). In the current paper, we are specifically focused on the amount of mass in the outflow. We, therefore, adopt the electron density scaling as done by Veilleux & Rupke (2002), where the mass outflow is normalized to $n_e = 100 \text{ cm}^{-3}$. We estimate that n_e introduces a systematic uncertainty of order 0.4–0.5 dex on the outflow mass. In a previous work, RC22 made a different assumption for n_e in order to compare with other observations. We discuss this further in Sections 3.3 and 3.4. To illustrate this systematic uncertainty, in Figures 2, 4, and 6, we include points that represent a higher n_e assumption

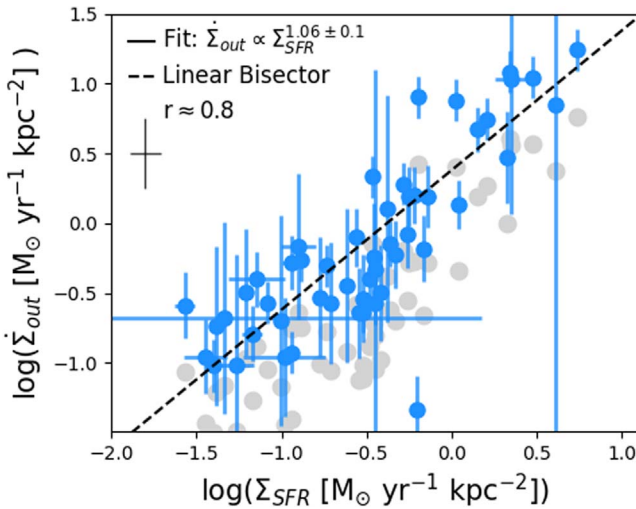


Figure 2. Ionized gas outflow mass flux ($\dot{\Sigma}_{\text{out}}$) compared to SFR surface density (Σ_{SFR}) for ~ 500 pc resolution pixels in IRAS08 where we have observed an outflow. The blue points are calculated assuming an n_e normalized to 100 cm^{-3} , and the faint gray points use an assumed $n_e = 300 \text{ cm}^{-3}$. A typical error bar is shown in the top left corner. We fit a relationship to the two quantities, which returns a slightly nonlinear correlation. Yet, within the scatter, the data is also consistent with a linear correlation (within 1.5σ).

as well as the $n_e = 100 \text{ cm}^{-3}$ assumption, as described in associated captions.

To calculate the SFR of each spaxel in IRAS08, we use the narrow line flux from the $\text{H}\beta$ fits, according to the conversion

$$\text{SFR} = C_{\text{H}\alpha} \left(\frac{L_{\text{H}\alpha}}{L_{\text{H}\beta}} \right) 10^{-0.4A_{\text{H}\beta}} L_{\text{H}\beta}. \quad (3)$$

Here, $C_{\text{H}\alpha} = 5.5335 \times 10^{-42} \text{ } M_{\odot} \text{ yr}^{-1} (\text{erg s}^{-1})^{-1}$, which assumes a Kroupa & Weidner (2003) initial mass function (IMF; Hao et al. 2011). $L_{\text{H}\alpha}/L_{\text{H}\beta} = 2.87$ is the luminosity ratio for electron temperature $T_e = 10^4 \text{ K}$ and case B recombination (Osterbrock & Ferland 2006). $A_{\text{H}\beta}$ is the extinction derived from the observed $\text{H}\beta/\text{H}\gamma$ ratios and a Calzetti (2001) attenuation curve. $L_{\text{H}\beta}$ is the observed $\text{H}\beta$ luminosity.

RC22 found the spatially resolved velocity, v_{out} , of the ionized gas outflow to be consistent with a shallow slope in $v_{\text{out}} \propto \Sigma_{\text{SFR}}^N$, with $N \propto 0.1\text{--}0.2$, similar to simulations (e.g., Kim et al. 2020). IRAS08 has an integrated mass-outflow rate in ionized gas of $\dot{M}_{\text{out}} \approx 7.9 \text{ } M_{\odot} \text{ yr}^{-1}$ and a corresponding ionized gas mass-loading factor of $\eta_{\text{ion}} = \dot{M}_{\text{out}}/\text{SFR} \approx 0.8$ when assuming $n_e = 380 \text{ cm}^{-3}$ (RC22). In RC22, the integrated mass-loading factor η_{ion} was calculated using SFRs from only those regions of IRAS08 where evidence of outflows is observed. These values of v_{out} , \dot{M}_{out} , and η are comparable to strong winds in well-studied local galaxies like NGC 253 (Bolatto et al. 2013a) and M82 (Shopbell & Bland-Hawthorn 1998), and suggest that the outflow is removing gas from the galaxy at comparable rates to the star formation.

2.3. NOEMA CO(2–1) Observations of Molecular Gas

CO(2–1) was observed in IRAS08 using the NOEMA Extended Millimeter Array (NOEMA) for 13 hr in the A configuration and 5.5 hr in the C configuration. Observations used the PolyFix correlator tuned to a sky frequency of 226.215 GHz in USB with a channel width of 2.7 km s^{-1} using nine antennas. We recover CO emission over twice the half-

light radius of the stars in IRAS08 ($r_{50} \sim 1 \text{ kpc}$ or $2.5''$) with a point-source sensitivity of $1.4 \text{ mJy beam}^{-1}$ in 20 km s^{-1} of bandwidth, and with a beam size of $0.52 \times 0.47 \text{ arcsec}^2$ ($\sim 197 \times 178 \text{ pc}^2$). For further details on the observations and data reduction, see F22.

To convert CO to H_2 , we consider both the metallicity and compactness of IRAS08 in selecting the appropriate conversion factor, α_{CO} . IRAS08 has a low metallicity ($0.7 Z_{\odot}$; López-Sánchez et al. 2006), indicating that a higher α_{CO} should be used. On the other hand, IRAS08 is also a compact and starbursting galaxy, suggesting a lower α_{CO} . Following the parameterizations from Bolatto et al. (2013b), these two properties offset each other in IRAS08. For simplicity's sake, we use a Milky Way $\alpha_{\text{CO}} = 4.36 \text{ } M_{\odot} (\text{K km s}^{-1} \text{ pc}^2)^{-1}$ corrected to the CO(2–1) transition using a line ratio of $R_{12} = \text{CO}(2\text{--}1)/\text{CO}(1\text{--}0) = 0.7$ such that $\alpha_{\text{CO}}^{2\text{--}1} = \alpha_{\text{CO}}/R_{12} = 6.23 \text{ } M_{\odot} (\text{K km s}^{-1} \text{ pc}^2)^{-1}$. The assumption of α_{CO} introduces a factor of $\sim 2\text{--}3$ systematic uncertainty in the gas mass surface density that is difficult to characterize further due to the competing effects of the metallicity and the starburst.

The molecular gas fraction of IRAS08 has been measured to be of order $f_{\text{gas}} \equiv M_{\text{mol}}/(M_{\text{star}} + M_{\text{mol}}) \sim 20\%$ (F22). Toomre's Q_{gas} characterizes the stability of a self-gravitating disk, where disks with high velocity dispersion are unstable if $Q_{\text{gas}} \leq 0.7$ (Romeo et al. 2010). Dynamically, F22 show that IRAS08 is consistent with a galaxy-wide violent disk instability (Dekel et al. 2009) with $Q_{\text{gas}} \sim 0.5$ across most of the disk, and high molecular gas velocity dispersions of $\sim 25\text{--}30 \text{ km s}^{-1}$.

F22 used NOEMA A+C observations of IRAS08 to study the star formation efficiency per freefall time, $\epsilon_{\text{ff}} \equiv \text{SFR}/(M_{\text{gas}} \times t_{\text{ff}})$, where the freefall time is $t_{\text{ff}} \equiv \sqrt{3\pi}/(32G\rho)$. They found at the 100 pc scale that ϵ_{ff} reaches high values in the galaxy center of $\sim 10\text{--}100\%$, which translates to a variable gas depletion time that decreases from $t_{\text{dep,SF}} \sim 1\text{--}2 \text{ Gyr}$ in the disk to $\sim 0.1 \text{ Gyr}$ in the galaxy center. The ϵ_{ff} found for IRAS08 by F22 is in the range of values expected from the models of Grudić et al. (2018), which we will discuss further in the context of outflows later in this paper. A strongly variable ϵ_{ff} is not well explained by current theory, and motivates our comparison to the impact that outflows may have on the star formation regulation.

2.4. Stellar Mass

We determine the stellar masses in $0.53 \times 0.57 \text{ kpc}$ regions by applying stellar population fits using the CIGALE code (Boquien et al. 2019) to HST/ACS image filters HRC F330W, WFC F435W, WFC F550M, and Spitzer/IRAC Ch1. Before fitting, all stellar continuum images are rotated, convolved to the matched point-spread function, and resampled to match the sampling of the KCWI data using Python routines. We remove backgrounds in all images by the standard process of fitting a simple surface to the images in galaxy emission-free regions. In the case of the HST images, the background is near zero. We only measure the stellar mass in regions of the image with significant detections of CO(2–1) and the outflow. This restricts the measurement to regions of the stellar continuum images with an $\text{S/N} \sim 50$ or higher in individual resolution elements.

To carry out the fitting, we assume the Calzetti et al. (2000) extinction law, allowing for a range of extinctions between $A_V \approx 0.05\text{--}2.0$. We note the typical extinction in IRAS08 is quite low, $A_V \approx 0.2\text{--}0.5$, similar to derivations from the Balmer

decrement. We follow the standard prescription for starburst galaxies as outlined in CIGALE papers (e.g., Boquien et al. 2019), and fit the star formation history (SFH) with a delayed starburst superimposed on an exponentially decaying SFR. The burst in each pixel is restricted to be less than 15% of the mass. Ambachew et al. (2022) studied the impact of the choice of SFH parameterization using CIGALE on derived stellar masses in galaxies similar to IRAS08, and find that it has only a small effect. Although we calculate the SFR assuming a Kroupa IMF, CIGALE only implements the Chabrier IMF, which has been shown to underestimate stellar mass-to-light ratios by 5%–10% in the ages that we expect for IRAS08 (Conroy et al. 2009). We, therefore, scale the derived masses by 1.08 to match the expected mass-to-light ratio of Kroupa IMFs (Conroy et al. 2009). We note that this is a minor adjustment compared to the systematic uncertainty in point-to-point measurements of stellar masses in high SFR galaxies. The typical mass-to-light ratio derived from this is of order $M/L_{3.6} \approx 0.1$ –0.3, which is consistent with similarly young, high SFR surface density systems (Ambachew et al. 2022). We find that the overall fit recovers a stellar mass of $\sim 1.1 \times 10^{10} M_{\odot}$ for the entire galaxy, which is similar to that reported elsewhere (e.g., López-Sánchez et al. 2006; Leitherer et al. 2013).

2.5. Prototype Outflow Galaxies for Comparison

We will compare the molecular gas surface density, Σ_{mol} , and the SFR surface density, Σ_{SFR} , from IRAS08 to literature values for outflow galaxies in the local universe (M82, NGC 253, and NGC 1482). For these galaxies throughout this work, we adopt values of Σ_{mol} and Σ_{SFR} that are intended to be from the area of the galaxy near the base of and likely driving the outflow, rather than the global galaxy integrated quantity. For M82, this corresponds to a kiloparsec-wide region, which has a molecular gas surface density of $\Sigma_{\text{mol}} \sim 250 M_{\odot} \text{ pc}^{-2}$ and SFR surface density of $\Sigma_{\text{SFR}} \sim 2.5$ –3 $M_{\odot} \text{ yr}^{-1} \text{ kpc}^{-2}$ (Kennicutt 1989; Leroy et al. 2015b).

For NGC 253, we use the values given by Leroy et al. (2015a) for the starbursting nuclear disk, $\Sigma_{\text{mol}} \sim 560 M_{\odot} \text{ pc}^{-2}$ and $\Sigma_{\text{SFR}} \sim 2.9 M_{\odot} \text{ yr}^{-1} \text{ kpc}^{-2}$.

For NGC 1482, we use the central kiloparsec values from Salak et al. (2020), $\Sigma_{\text{mol}} \sim 490 M_{\odot} \text{ pc}^{-2}$ and $\Sigma_{\text{SFR}} \sim 1.3 M_{\odot} \text{ yr}^{-1} \text{ kpc}^{-2}$.

Note that values of the local outflows (M82, NGC 253, and NGC 1482) are only used for context. We never include them in fitting relationships.

3. Relationship between Molecular Gas Depletion and Outflows

3.1. $\dot{\Sigma}_{\text{out}}$ and Σ_{SFR}

The outflow mass flux is defined as the mass-outflow rate normalized by the surface area of the measurement, $\dot{\Sigma}_{\text{out}} = \dot{M}_{\text{out}} / \text{Area}$. This quantity is described in Kim & Ostriker (2017), and is useful for resolved outflow studies. We show the ionized gas outflow mass flux, $\dot{\Sigma}_{\text{out}}$, for IRAS08 found using observations with KCWI/Keck II as shown in Figure 1. Our NOEMA observations were not deep enough to detect broad line emission that could be associated with the molecular component of the outflow.

It is commonly expected that a higher SFR surface density, Σ_{SFR} , drives a higher mass-outflow rate, \dot{M}_{out} (e.g., Hopkins et al. 2012; Arribas et al. 2014; Heckman et al. 2015; Muratov

et al. 2015; Hayward & Hopkins 2017; Roberts-Borsani et al. 2020). In Figure 2, we plot $\dot{\Sigma}_{\text{out}}$ against Σ_{SFR} for IRAS08 at an ~ 500 pc sampling scale.

In IRAS08, we measure $\dot{\Sigma}_{\text{out}} \sim 0.1 M_{\odot} \text{ yr}^{-1} \text{ kpc}^{-2}$ to $\sim 15 M_{\odot} \text{ yr}^{-1} \text{ kpc}^{-2}$ over 2 orders of magnitude in Σ_{SFR} (Figure 2). We find a Pearson correlation coefficient of $r = 0.8$ (p -value = 6×10^{-13}) for $\log(\Sigma_{\text{SFR}}) - \log(\dot{\Sigma}_{\text{out}})$. There is a large range in error bars on $\dot{\Sigma}_{\text{out}}$, which would bias the fit to those few points at high S/N. We, therefore, place a minimum uncertainty of 0.15 dex on $\dot{\Sigma}_{\text{out}}$ for the fit. Using the method of orthogonal distance regression, we find the fit to be

$$\dot{\Sigma}_{\text{out}} = 10^{0.43 \pm 0.06} \Sigma_{\text{SFR}}^{1.06 \pm 0.10}. \quad (4)$$

In Figure 2, we also show the linear bisector. If we do not constrain the error bars, the fit returns a slightly nonlinear power law of $\dot{\Sigma}_{\text{out}} \propto \Sigma_{\text{SFR}}^{1.12 \pm 0.09}$. The rms deviation of the fit is essentially equivalent to the rms of the bisecting line, at 0.36 dex. Therefore, while the regression to the unconstrained error bars returns a slightly nonlinear fit, our results are consistent with a linear relationship $\dot{M}_{\text{out}} \propto \Sigma_{\text{SFR}}$ (within 1.5σ).

While there are no observational measurements that we are aware of that compare $\dot{\Sigma}_{\text{out}}$ to Σ_{SFR} , there are some studies that investigate correlations between the integrated star formation and outflow mass rates (e.g., Heckman et al. 2015). We note that there are significant differences between these measurements. We are measuring $\dot{\Sigma}_{\text{out}}$ and Σ_{SFR} in ionized gas in equally sized areas in a single galaxy at a fixed distance. Fluetsch et al. (2019) found a slightly nonlinear relationship, $\dot{M}_{\text{out}} \propto \text{SFR}^{1.19 \pm 0.16}$, for molecular gas outflows in local star-forming galaxies. Avery et al. (2021) found a similar linear slope of $\dot{M}_{\text{out}} \propto \text{SFR}^{0.97 \pm 0.07}$ for integrated outflows on MaNGA galaxies using $\text{H}\alpha$ to measure outflows.

To compare to our results from IRAS08, we calculate the mass-outflow rate in ionized gas of M82 and NGC 1482 from the total $\text{H}\alpha$ luminosity and outflow velocity using values from Shopbell & Bland-Hawthorn (1998) and Veilleux & Rupke (2002), respectively. For each of these, we assume, as we do for IRAS08, $n_e \approx 100 \text{ cm}^{-3}$ and $R_{\text{out}} = 0.5 \text{ kpc}$. We find ionized gas mass-outflow rates of $\sim 2 M_{\odot} \text{ yr}^{-1}$ for M82 (Shopbell & Bland-Hawthorn 1998) and $\sim 0.6 M_{\odot} \text{ yr}^{-1}$ for NGC 1482 (Veilleux & Rupke 2002). These \dot{M}_{out} values translate to $\dot{\Sigma}_{\text{out}} \approx 2.5 M_{\odot} \text{ yr}^{-1} \text{ kpc}^{-2}$ for M82, and $\sim 0.75 M_{\odot} \text{ yr}^{-1} \text{ kpc}^{-2}$ for NGC 1482. We note these are measured in edge-on systems and are thus quite different methods of estimating the mass-outflow rate. Nonetheless, they are in the range of what we measure for the high Σ_{SFR} regions in IRAS08 (see Figure 2).

The relationship between Σ_{SFR} and Σ_{mol} we observe in IRAS08 is broadly consistent with both theoretical expectations and observations of entire galaxies. In the subsequent analysis, it will be important to keep track of when the fundamental driver of any relationship may be a reflection of this strong correlation in Figure 2.

3.2. Connecting the $\Sigma_{\text{mol}} - \Sigma_{\text{SFR}}$ Relationship to Outflows

There is a long history of literature discussing the resolved observations of the relationship between Σ_{SFR} and the molecular gas surface density, Σ_{mol} , in galaxies (Kennicutt 1989; Bigiel et al. 2008; Genzel et al. 2011; Kennicutt & Evans 2012; Leroy et al. 2013) and theories explaining it (Ostriker et al. 2010; Faucher-Giguère et al. 2013; Hayward &

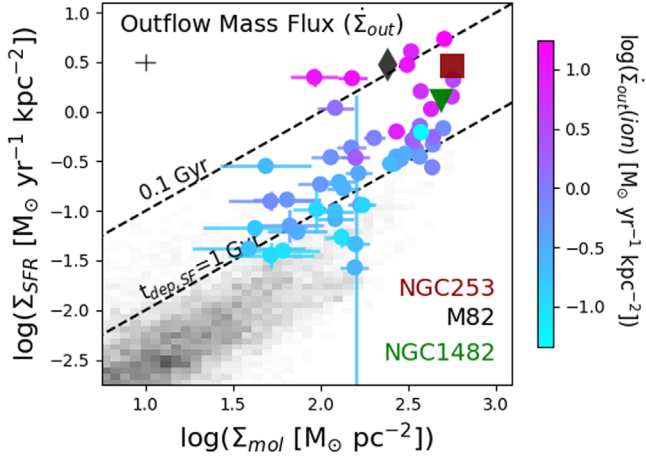


Figure 3. The resolved relationship between SFR surface density, Σ_{SFR} , and molecular gas surface density, Σ_{mol} . The circles of IRAS08 are colored according to the mass-outflow flux, $\dot{\Sigma}_{\text{out}}$. Note that the vertical blue line denotes the largest of the Σ_{SFR} error bars, and the rest of the error bars are smaller than the points. A typical error bar is shown in the top left corner. The gray points represent data from the HERACLES sample of local spirals (Leroy et al. 2013). NGC253 (Bolatto et al. 2013a), M82 (Leroy et al. 2015b), and NGC1482 (Veilleux & Rupke 2002; Salak et al. 2020) are represented as a dark red square, a black diamond, and a green triangle, respectively. The dashed lines indicate where the time it takes to deplete the molecular gas through star formation, $t_{\text{dep,SF}}$, would be 0.1 Gyr (top line) and 1.0 Gyr (bottom line). In IRAS08, a greater distance from the spiral sequence (gray points) in $\Sigma_{\text{SFR}}-\Sigma_{\text{mol}}$ corresponds to outflows with higher mass-outflow rates and higher momentum flux.

Hopkins 2017; Krumholz et al. 2018). F22 recently analyzed the resolved molecular gas depletion timescale for IRAS08. They find it is consistent with a steep power-law slope for $\Sigma_{\text{SFR}} \propto \Sigma_{\text{mol}}^N$, with $N \approx 1.5-1.6$, similar to starburst outflow systems like NGC 253, M82, and NGC 1482.

In Figure 3, we show the relation between Σ_{SFR} and the molecular gas surface density, Σ_{mol} , for IRAS08 in ~ 0.5 kpc sampling scale. The high Σ_{SFR} center of IRAS08 is comparable in both Σ_{SFR} and Σ_{mol} to other well-known outflow galaxies in the local universe (NGC 253, M82, and NGC 1482).

We color the IRAS08 points by $\dot{\Sigma}_{\text{out}}$. In Figure 2, we showed a tight correlation between $\dot{\Sigma}_{\text{out}}$ and Σ_{SFR} . However, it is clear from Figure 3 that there is a large spread in Σ_{mol} for a given value of $\dot{\Sigma}_{\text{out}}$. The Pearson correlation coefficient is $r = 0.8$ (p -value = 6×10^{-13}) for $\log(\dot{\Sigma}_{\text{out}})-\log(\Sigma_{\text{SFR}})$. This reduces significantly to $r = 0.5$ (p -value = 4×10^{-4}) for $\log(\dot{\Sigma}_{\text{out}})-\log(\Sigma_{\text{mol}})$.

The average error on the Σ_{SFR} points is 0.06 dex. This typically small value is due to the very high S/N of the KCWI data. One point in Figures 2 and 3 shows a much larger error, and comes from a measurement made with a lower S/N than the remainder of the galaxy.

Figure 3 shows a clear trend that regions of IRAS08 with shorter molecular gas depletion times (indicated by the dashed lines) have larger values of $\dot{\Sigma}_{\text{out}}$, as indicated by the colored points. A power-law fit to the relationship yields a power-law slope that is close to linear, and is likely driven by the correlation in Figure 2. We find

$$\dot{\Sigma}_{\text{out}} = 10^{9.2 \pm 0.5} t_{\text{dep}}^{-1.1 \pm 0.06} \quad (5)$$

with a correlation coefficient of $r = -0.85$ and a p -value of roughly 10^{-16} .

We can also estimate the momentum flux, defined as $dp/dt \equiv v_{\text{out}} \dot{M}_{\text{out}}$. We do not plot these values because dp/dt is primarily determined by \dot{M}_{out} and therefore has a dependency that is nearly identical to that of $\dot{\Sigma}_{\text{out}}$. The momentum flux we measure increases from $\sim 10^{0.7}$ to $\sim 10^{3.2} M_{\odot} \text{ km s}^{-1} \text{ yr}^{-1}$. The highest values of dp/dt are similar to what is derived for molecular gas in M82 (Leroy et al. 2015b). The correlation for IRAS08 between the momentum flux and the star formation depletion time is significant and nonlinear (Pearson correlation coefficient $r = -0.7$, p -value = 2×10^{-9}), implying that regions in IRAS08 that are more efficient at turning gas into stars are increasingly more efficient at generating significant momentum in the outflow.

3.3. Outflow Efficiency

In Figure 4, we compare $\dot{\Sigma}_{\text{out}}/\Sigma_{\text{mol}}$, which we refer to as the *outflow efficiency* of ionized gas, to $\Sigma_{\text{SFR}}/\Sigma_{\text{mol}}$ and to the unnormalized SFR surface density (Σ_{SFR}). The outflow efficiency may be interpreted as the rate at which the outflow exhausts the gas mass with the measured mass-outflow rate (assuming there is no supply of fresh gas). We will refer to $\Sigma_{\text{SFR}}/\Sigma_{\text{mol}}$ as the star formation efficiency for ease of discussion, noting the important distinction between this quantity and the star formation efficiency per freefall time (discussed in F22).

In the left panel of Figure 4, we compare the outflow efficiency to the star formation efficiency. When outflow efficiency is greater than star formation efficiency this suggests that outflows more rapidly remove gas from the local region than does the conversion of gas into new stars. We note that the ratio of these two quantities gives the more well-known metric, the mass-loading factor η , which we will consider in Section 3.4. In IRAS08, the average $\log(\dot{\Sigma}_{\text{out}}/\Sigma_{\text{mol}} [\text{yr}^{-1}]) = -8.4$ with a standard deviation of 0.55 dex. We find that 87% of measured regions in IRAS08 fall above the one-to-one line in this space, with a median ratio of ~ 2.4 , when assuming $n_e = 100 \text{ cm}^{-3}$. This is similar to unresolved observations of similar quantities, $t_{\text{dep,out}}$ and $t_{\text{dep,SF}}$, in Fluetzsch et al. (2019). For star-formation-driven winds in eight galaxies, they found that the galaxies have longer star formation depletion times (smaller $\Sigma_{\text{SFR}}/M_{\text{mol}}$) in those galaxies with longer outflow depletion times (smaller $\dot{M}_{\text{out}}/M_{\text{mol}}$).

We find the outflow efficiency and star formation efficiency are correlated with a Pearson correlation coefficient of $r = 0.7$ (p -value = 6×10^{-10}). We find the resulting fit, by the method of error-weighted orthogonal distance regression, to be

$$\frac{\dot{\Sigma}_{\text{out}}}{\Sigma_{\text{mol}}} = 10^{3.5 \pm 1.2} \left(\frac{\Sigma_{\text{SFR}}}{\Sigma_{\text{mol}}} \right)^{1.35 \pm 0.14}. \quad (6)$$

This steeper-than-linear slope suggests that in regions of high star formation efficiency, the outflow dominates slightly more than it does in regions with star formation similar to that in typical spiral disks. Note that a typical depletion time of ~ 2 Gyr, as is found in spirals (Leroy et al. 2013), corresponds to a star formation efficiency of -9.3 dex as shown in Figure 4. It is technically challenging, with present-day instrumentation, to observe outflows in typical spirals due to the lower \dot{M}_{out} and smaller velocity offset (e.g., Roberts-Borsani et al. 2020). Moreover, in the main disks of spirals the ratio of $\Sigma_{\text{SFR}}/\Sigma_{\text{mol}}$ changes by less than 20% with the Galactocentric distance

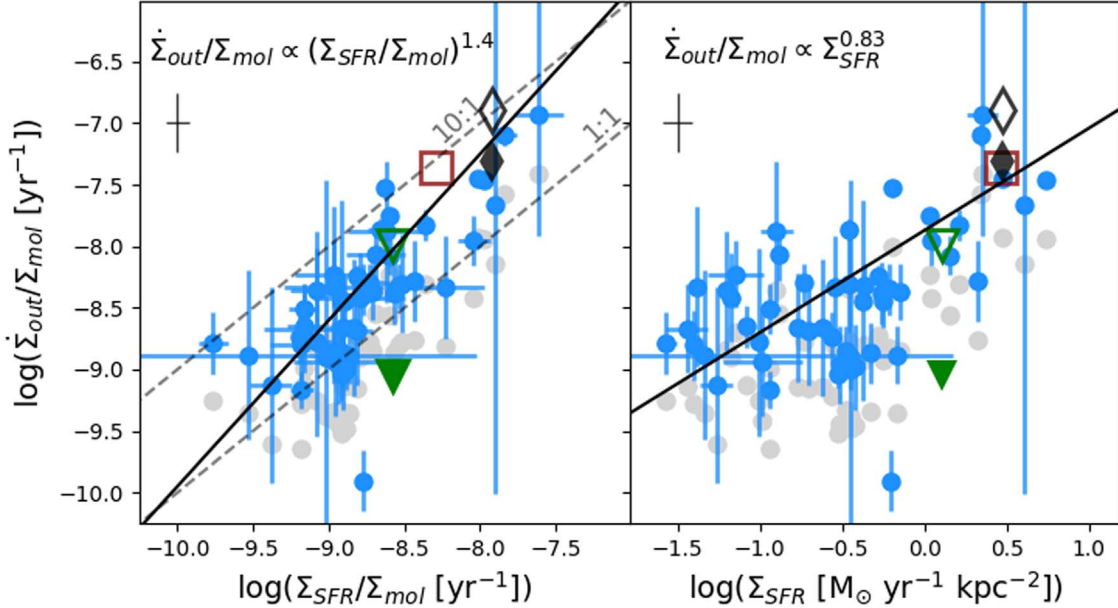


Figure 4. The outflow efficiency $\dot{\Sigma}_{\text{out}}/\Sigma_{\text{mol}}$ of IRAS08 plotted against the star formation efficiency $\Sigma_{\text{SFR}}/\Sigma_{\text{mol}}$ (left), and SFR surface density Σ_{SFR} (right). In both panels, the blue circles represent our IRAS08 data using $n_e = 100 \text{ cm}^{-3}$. Fainter gray circles represent IRAS08 if an electron density of $n_e = 300 \text{ cm}^{-3}$ were used. A typical error bar is shown in the top left corner. M82, the central kiloparsec of NGC 1482, and the center of NGC 253 are denoted by the black diamond, green triangle, and dark red square, respectively. Open symbols for these galaxies indicate the results for the molecular gas mass-outflow rate, and filled-in symbols indicate the ionized gas mass-outflow rate. In the left panel, the 1:1 and 10:1 ratios of the outflow efficiency to star formation efficiency are plotted as gray dashed lines. A fit to the IRAS08 data is given by the solid black line. In the right panel, the solid black line shows a fit of the outflow efficiency to Σ_{SFR} . In high Σ_{SFR} regions, IRAS08 drives more efficient outflows.

within 8 kpc, not including the galactic nucleus (Leroy et al. 2013). It is, therefore, not clear how this relationship would behave in the disks of spiral galaxies.

We note that the systematic uncertainty introduced from n_e would not necessarily change the trend; however, it may imply that the ionized gas outflow efficiency is more comparable to the star formation efficiency. If the n_e of the outflow changes with Σ_{SFR} within a galaxy, this would alter the slope shown in Figure 4, but we do not have any results to suggest whether this occurs. Another large systematic uncertainty, however, is the ratio of the outflow mass flux in different phases, specifically the ionized-to-molecular gas ratio. Molecular gas is the more dominant phase of outflow mass (review Veilleux et al. 2020), which increases the total \dot{M}_{out} by a factor of $\sim 5\text{--}10\times$ (Fluetsch et al. 2019; Herrera-Camus et al. 2020). This suggests that even with a higher n_e , outflows likely dominate over star formation in removing the gas in the starbursting center of IRAS08. If the ratio of ions to molecules changes with Σ_{SFR} this too would affect the relationship between the outflow efficiency and star formation efficiency. In four galaxies, Fluetsch et al. (2019) found a relatively constant relationship between the mass-outflow rate measured in ions compared to molecules.

In the right panel of Figure 4, we compare outflow efficiency to the SFR surface density. There is likewise a positive correlation between the quantities such that outflows colocated with regions of high Σ_{SFR} have higher efficiency. We find a correlation coefficient of $r \approx 0.5$ (p -value = 8×10^{-5}). We find that

$$\frac{\dot{\Sigma}_{\text{out}}}{\Sigma_{\text{mol}}} = 10^{-7.86 \pm 0.05} \Sigma_{\text{SFR}}^{0.83 \pm 0.11}. \quad (7)$$

We can compare this correlation to that shown in Figure 2, which has a steeper power law, higher correlation coefficient,

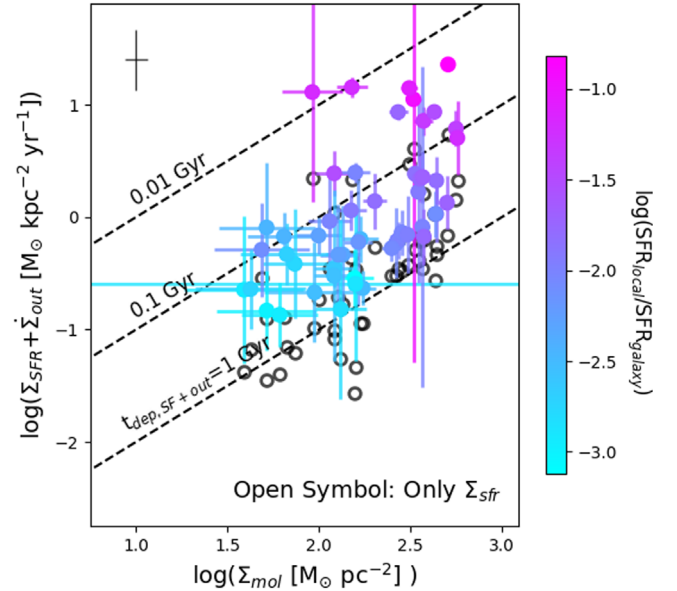


Figure 5. The combined $\Sigma_{\text{SFR}} + \dot{\Sigma}_{\text{out}}$ is compared to Σ_{mol} for regions in IRAS08, and shown as the solid points. Colors indicate the fraction of the total SFR in the corresponding area. A typical error bar is shown in the top left corner. The combined SFR and outflow mass flux represent a more complete view of gas removal. Open symbols represent only Σ_{SFR} for comparison. In lower Σ_{SFR} regions the combination only makes a factor ~ 2 change to the gas depletion time (dashed lines), but at high Σ_{SFR} it decreases the total depletion time by nearly an order of magnitude.

and less scatter in the fit as indicated by the fit uncertainties. The larger correlation coefficient implies that the inclusion of the galactic disk molecular gas mass in the outflow efficiency increases the scatter shown in Figure 4.

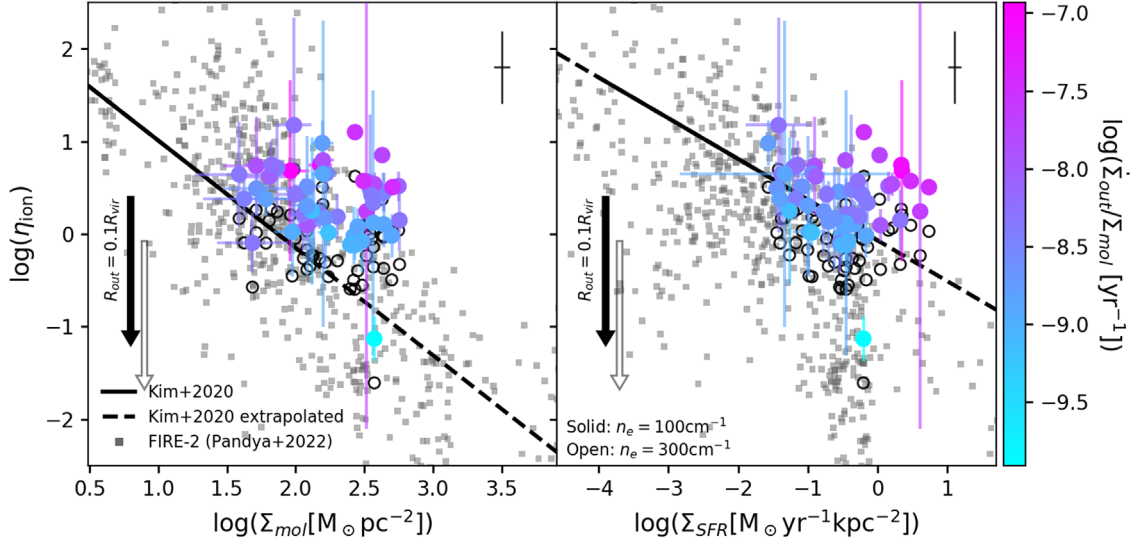


Figure 6. The mass-loading factor of ionized gas, η_{ion} , as a function of the molecular gas surface density, Σ_{mol} (left panel) and the SFR surface density, Σ_{SFR} (right panel). Observational data from IRAS08 is given in circles colored by outflow efficiency using $n_e = 100 \text{ cm}^{-3}$, with rescaled values for an electron density of $n_e = 300 \text{ cm}^{-3}$ as open circles. The black arrows show the magnitude and direction the median η_{ion} value would move if we assumed an outflow extent of $R_{\text{out}} = 0.1 R_{\text{vir}}$ (open arrow represents the median with $n_e = 300 \text{ cm}^{-3}$). Typical error bars for the IRAS08 data are shown in the top right corner of each panel. We compare our observational results from IRAS08 with results from the FIRE-2 (Pandya et al. 2021, Figure 11) and TIGRESS (Kim et al. 2020, Figure 9) simulations. Results from the warm-phase gas ($10^3 < T < 10^5 \text{ K}$) from FIRE-2 are shown as gray squares. The $\Sigma_{\text{mol}}-\eta_{\text{ion}}$ and $\Sigma_{\text{SFR}}-\eta_{\text{ion}}$ relationships found in Kim et al. (2020) for the cool gas component ($T < 2 \times 10^4 \text{ K}$) are plotted with solid black lines, and extrapolated past the parameter space they covered with the dashed black lines. The simulation data is not inconsistent with our observational results.

In Figure 5, we compare the molecular gas surface density to the combination of both the SFR surface density and outflow mass flux. The combination of $\Sigma_{\text{SFR}} + \dot{\Sigma}_{\text{out}}$ can be thought of as a more complete estimate of the removal of gas from the star-forming region, noting of course that the addition of molecular outflows is needed for a full accounting of the outflow mass. The figure clearly demonstrates that the addition of both the Σ_{SFR} and $\dot{\Sigma}_{\text{out}}$, together, shortens the depletion time significantly in the high Σ_{SFR} regions by nearly an order of magnitude.

Similar to the depletion time measured with only the star formation, the combination of outflow and star formation results in a depletion time that varies within the galaxy and with local Σ_{SFR} . This is not surprising given our result shown in Figure 2 that $\dot{\Sigma}_{\text{out}} \propto \Sigma_{\text{SFR}}$. We find for radii within 1 kpc the median outflow+star formation depletion time ($\Sigma_{\text{mol}}/(\dot{\Sigma}_{\text{out}} + \Sigma_{\text{SFR}})$) is of order 0.05 Gyr. We find a similar value if we select those regions with $\Sigma_{\text{SFR}} > 1 M_{\odot} \text{ yr}^{-1} \text{ kpc}^{-2}$. This depletion time increases to 0.3 Gyr for larger radii and lower Σ_{SFR} . We note that while 1 kpc is a small area, it represents over 50% of the total star formation in the galaxy, as indicated by the colors in Figure 5.

We reiterate that the main systematic uncertainty in our results is that the observations of outflows are only of a single phase, and that the addition of the molecular phase could increase the outflow mass rate by as much as an order of magnitude. This would reduce the total depletion time to only 0.005–0.01 Gyr in the center of IRAS08, which is very short, and is comparable to the freefall time found for these regions (F22).

3.4. Mass-loading Factors

In Figure 6 we compare the mass-loading factor, $\eta_{\text{ion}} = \dot{\Sigma}_{\text{out}}/\Sigma_{\text{SFR}}$, to Σ_{mol} and Σ_{SFR} in IRAS08. We additionally overplot results from the recent FIRE-2 simulations

(Pandya et al. 2021) and the SMAUG-TIGRESS simulation (Kim et al. 2020). A number of simulations and analytic theories predict a decreasing η_{ion} with increasing Σ_{SFR} (recently Fielding et al. 2017; Li et al. 2017; Kim et al. 2020; Pandya et al. 2021). Observations are mixed as to how well these correlate (Arribas et al. 2014; Roberts-Borsani et al. 2020).

In IRAS08, we find very little correlation between η_{ion} and Σ_{mol} . We find a Pearson correlation coefficient of $r = -0.23$ (p -value = 0.1) for $\log(\Sigma_{\text{mol}}) - \log(\eta_{\text{ion}})$. We note, however, that these values of Σ_{mol} in IRAS08 cover a fairly small range compared to the FIRE-2 simulations. We also note that the FIRE-2 simulations calculate the total values of η and Σ_{mol} for entire galaxy halos, rather than resolved regions. Moreover, the values of IRAS08, while being on the high side of the FIRE-2 data and over the Kim et al. (2020) correlation, are not completely discrepant. Nevertheless, our data are consistent with no correlation between η and Σ_{mol} . This is in contrast to the steeper trend expected from both the TIGRESS and FIRE-2 simulations (Kim et al. 2020; Pandya et al. 2021). It could be that we should expect different relations when comparing our resolved observations to simulations on different spatial scales. In order to recover the high scatter correlation that simulations predict between η_{ion} and Σ_{mol} , we may need to include observations of more galaxies covering a larger range in Σ_{mol} .

For $\log(\Sigma_{\text{SFR}}) - \log(\eta_{\text{ion}})$ we similarly find a weak-to-no trend (Pearson correlation coefficient of $r = -0.17$, p -value = 0.23). We note that below $\log(\Sigma_{\text{SFR}}[M_{\odot} \text{ yr}^{-1} \text{ kpc}^{-2}]) \approx -0.5$ the data in IRAS08 is much more consistent with the theoretical expectations from Kim et al. (2020) and is consistent with a negative correlation (correlation coefficient of $r = -0.67$, p -value = 2.5×10^{-4}). It is possible that regions of the galaxy below this Σ_{SFR} follow the predicted relationship, but that in regions with higher Σ_{SFR} the outflow efficiency increases (see Figure 4) and we therefore observe a flat η_{ion} . It is important to also point out that the simulations of Kim et al.

(2020) are only run to $\Sigma_{\text{SFR}} \sim 1.0 M_{\odot} \text{ yr}^{-1} \text{kpc}^{-2}$ and to $\Sigma_{\text{mol}} \sim 100 M_{\odot} \text{ pc}^{-2}$. We have extrapolated their $\Sigma_{\text{mol}}-\eta_{\text{ion}}$ and $\Sigma_{\text{SFR}}-\eta_{\text{ion}}$ relations past this parameter space in order to compare to our observations of a starbursting environment. It is unclear whether this extrapolation should hold in starbursting environments.

We note that the systematic uncertainty of n_e is such that assuming higher values of n_e would bring our observed $\Sigma_{\text{mol}}-\eta_{\text{ion}}$ into better agreement with the Kim et al. (2020) prediction. This would, however, simultaneously make the mass-loading factors too low in comparison to Σ_{SFR} .

While we observe the molecular gas surface density Σ_{mol} , the TIGRESS simulations measure the total ISM gas mass divided by the horizontal area of the disk included in the box of the simulation. Their horizontal box sizes range from 512–2048 pc. The largest of these is $\sim 4 \times$ the area of our pixels. Moreover, we need to be mindful that the comparison to the FIRE-2 results is not an apples-to-apples comparison. Pandya et al. (2021) defined particles as outflows if they flow away from the galaxy disk and reach $0.1R_{\text{vir}}$ with enough energy remaining to make it to a larger radius. To convert the down-the-barrel observations of outflows into a mass-outflow rate we assume an *outflow radius* of $R_{\text{out}} = 500$ pc for our target (for more details, see RC22). This is $4 \times$ smaller than the $0.1R_{\text{vir}}$ used by Pandya et al. (2021), which would be ~ 20 kpc for a galaxy of IRAS08's mass. We do not know how the velocity and density profiles of the outflow change with radius; however, assuming everything stays the same, we rescale our data to use $R_{\text{out}} = 20$ kpc. Rescaling our data decreases the median value of η_{ion} from 2.5–0.06. This rescaling introduces significant uncertainty. It would be useful in the future for simulations to estimate the properties of outflows such as the mass-loading factor of the warm ionized gas in the region less than 10 kpc from the galaxy disk, where we observationally measure outflow properties.

3.5. Breakout Outflows

In a series of papers, Orr et al. (2022a, 2022b) considered the impacts of supernova clustering on the regulation of star formation by stellar feedback, and the conditions in which supernovae leave the disk or impart their momentum to the ISM. They outlined the scenarios in which a resulting superbubble generated by a supernova explosion expands until it either breaks out of the galaxy disk, or stalls within the galaxy. This simple, yet predictive, model is motivated by and is consistent with simulations of outflows (Fielding et al. 2018) and star cluster formation (Grudić et al. 2018). As the authors define it, in the event of *breakout*, more than 60% of the momentum from the subsequent supernovae transfers to the outflow rather than coupling to the ISM.

Orr et al. (2022b) put forward the prediction that a boundary line exists in the parameter space between local gas fraction, $f_{\text{gas}} \equiv \Sigma_{\text{gas}}/(\Sigma_{\text{gas}} + \Sigma_{\text{star}})$, and the orbital frequency, $\Omega \equiv v(R)/R$, that determines whether an outflow travels beyond the vertical scale height of the disk (i.e., breakout) or stays bound inside the disk (i.e., stalled) (see also Orr et al. 2022a).

We compare our observations for IRAS08 to the predictions from Orr et al. (2022a) in Figure 7. We find that the vast majority ($\sim 85\%$) of our resolved regions in IRAS08 have f_{gas} and Ω consistent with the predicted region for breakout outflows. We take the velocity models used in F22 for IRAS08, in which a flat rotation curve is fit to the CO(2–1) data, such

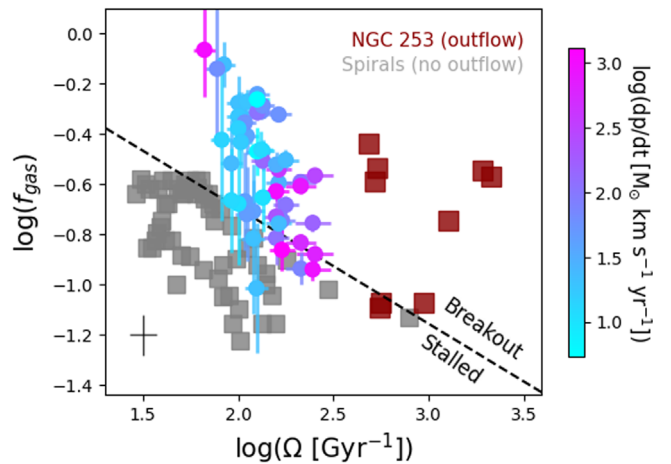


Figure 7. The gas fraction, $f_{\text{gas}} \equiv \Sigma_{\text{mol}}/(\Sigma_{\text{mol}} + \Sigma_{\text{star}})$, is compared to the orbital frequency, Ω . Data points for IRAS08 are colored by the outflow momentum flux, dp/dt . A typical error bar for the IRAS08 data is shown in the bottom left corner. The dashed line shows the boundary predicted by Orr et al. (2022a) between outflows that breakout of the disk, and outflows that are stalled within the disk (see their Figures 1 and 2). Gray squares indicate resolved observations of local spiral galaxies with no observed outflow. Red squares indicate the resolved observations of the outflow in NGC 253. We find that $\sim 85\%$ of our resolved regions are within the predicted region for breakout outflows.

that $v(R) = v_{\text{flat}}[1 - \exp(-R/r_{\text{flat}})]$. There is a significant systematic uncertainty in IRAS08 due to the low inclination of the galaxy. We adopt $i \approx 20^\circ$, which F22 derived from the HST/F550M isophotes at large radius, which is similar to the assumed inclination in Leitherer et al. (2013). An uncertainty in the inclination angle of $\pm 5^\circ$ would result in an uncertainty in Figure 7 of ± 0.15 dex in $\log(\Omega)$. Observationally this produces a challenging balance, as outflows would become more difficult to observe in more highly inclined systems. The figure also compares the IRAS08 measurements to NGC 253, which is known to contain an outflow. Given that we have thus far seen similar behavior between NGC 253 and IRAS08, it is therefore further consistent that both are above the breakout line. Moreover, as a control (Orr et al. 2022a, see their Figure 1) showed data for four spiral galaxies that are known to not have outflows, which we show are not colocated with IRAS08.

We can compare the outflow velocity in IRAS08 to local velocity dispersion to check if the Orr et al. (2022a, 2022b) breakout scenario is consistent with outflows moving beyond the scale height of the disk. The scale height of a disk is set by $h_z \propto \sigma^2/\Sigma_{\text{gas}}$, where σ is the velocity dispersion (see the discussion in Wilson et al. 2019). For standard scenarios, if an outflow is moving faster than σ , it will reach the scale height of the disk. F22 showed that the velocity dispersion of the molecular gas is on average $25 \pm 6 \text{ km s}^{-1}$, with the highest values being $\sim 40 \text{ km s}^{-1}$. The minimum of our estimated outflow velocities, v_{out} , is of order 130 km s^{-1} , which is well above the dispersion of the disk, even if we account for systematic differences between ionized and molecular gas velocity dispersions (Girard et al. 2021). The position of IRAS08 in the $f_{\text{gas}}-\Omega$ diagram is therefore consistent with the theory put forward in Orr et al. (2022b). We can also argue that this implies the depletion of gas discussed in previous sections is indeed leaving the plane of the disk, and removing gas from star formation.

Orr et al. (2022b) also predicted that at fixed f_{gas} and larger Ω less momentum couples to the gas in the disk, and more

momentum couples to the outflow. For every unit of new stellar mass that is formed, there is an amount of momentum that is available to be coupled to the surrounding gas (ISM or outflow). We do not know the exact relationship between our observable outflow momentum flux, dp/dt , and the amount of momentum per unit of new stellar mass formed, p/m_* . While we cannot observe the momentum that couples to the ISM gas, we can observe the momentum flux of the outflow in each region. In Figure 7, we color the points of IRAS08 by their outflow momentum flux. We find that increasing Ω corresponds with increasing momentum flux within the outflow, i.e., outflows launched closer to the galaxy center have greater momentum. Note that to first order dp/dt simply traces \dot{M}_{out} , we therefore expect similar correlations with $\dot{\Sigma}_{\text{out}}$. There are a number of uncertainties, not the least of which is likely the phase distribution of the momentum of the outflow (see Fielding & Bryan 2022 for an in-depth theoretical exploration of the momentum content of multiphase galactic winds). Nonetheless, it is plausible that as more momentum flux is incorporated in the outflow this would imply that less is available to generate turbulence in the ISM. The effect is thus to decrease the effective p/m_* felt by the disk surrounding the outflow.

4. Summary and Discussion

4.1. Summary

We present resolved measurements of IRAS08 in ionized gas using KCWI/Keck and molecular gas using NOEMA. We use these observations to relate the molecular gas mass and star formation observed in the galaxy to the resolved outflow and its properties. We have shown that the combined comparison of Σ_{SFR} , Σ_{mol} , and $\dot{\Sigma}_{\text{out}}$ allows for a very direct comparison to theory, in which three parameters that are thought to combine to regulate star formation in disk galaxies are characterized.

We have shown a direct correlation between the resolved Σ_{SFR} and the colocated outflow mass flux, $\dot{\Sigma}_{\text{out}}$, in regions of ~ 500 pc. We find that $\dot{\Sigma}_{\text{out}}$ correlates much more strongly with Σ_{SFR} than Σ_{mol} . This leads to a connection between outflow strength and location in the Kennicutt–Schmidt relationship between $\Sigma_{\text{SFR}}-\Sigma_{\text{mol}}$, such that regions of the galaxy with shorter molecular gas depletion times have stronger outflows. There is therefore a strong, superlinear relationship between the outflow efficiency $\dot{\Sigma}_{\text{out}}/\Sigma_{\text{mol}}$ and the inverse of the gas depletion time $t_{\text{dep}}^{-1} = \Sigma_{\text{SFR}}/\Sigma_{\text{mol}}$.

We find that the mass-loading factors we observe are consistent with predictions from multiple simulations (Kim et al. 2020; Pandya et al. 2021). The outflows we resolve are consistent with breakout outflows according to the region in the $f_{\text{gas}}-\Omega$ plane defined by Orr et al. (2022a, 2022b). For our galaxy, we can compare the velocity of the outflow to the local velocity dispersion, which we indeed find is consistent with outflows traveling fast enough to leave the disk.

4.2. Systematic Uncertainties

In this paper, we attempt to derive physical quantities of outflows from observations. This is necessary to compare to theory and simulation; however, the derivation is heavily impacted by assumptions that introduce systematic uncertainties. We do not have strong constraints on how the n_e of the outflow changes across either a range of galaxies, or for regions within a galaxy. Moreover, outflows are clearly multiphase

phenomena (e.g., Fluetsch et al. 2019; Herrera-Camus et al. 2020; Fluetsch et al. 2021). However, the ratio of the mass-outflow rate in ions to other phases of gas is not well constrained by observations, especially on resolved scales within galaxies. Leroy et al. (2015b) provided a heuristic model in which this ratio could change based on the local region of the galaxy. More work constraining these properties with ALMA, MUSE, and KCWI is direly needed in order to reduce these systematics, and confirm the results we have presented.

4.3. Implications for Star Formation Regulation in High Σ_{SFR} Galaxies

The superlinear relationship between outflow efficiency and star formation efficiency (Figure 4) has implications for how galaxies regulate their star formation. This correlation suggests that in the disk mode of star formation, the outflow and the star formation are similarly effective at removing gas, thus regulating the ability to form new stars. However, as the disk moves into a starburst mode, this regulation becomes more dominated by the outflow.

We can therefore outline a picture in which the nature of the mechanism regulating star formation may change with respect to location in the $\Sigma_{\text{SFR}}-\Sigma_{\text{mol}}$ plane. At a fixed Σ_{mol} , as the Σ_{SFR} increases above the typical depletion time of ~ 1 –2 Gyr, the outflows become the dominant mechanism in removing gas. Krumholz et al. (2018) argue that gas inflow rates in disks are comparable to the SFR, and therefore if the mass-outflow rate becomes significantly greater than $\eta \sim 1$, as we show in Figure 6, then the gas removal by the outflow will reduce the gas surface density. This then causes the SFR surface density to decline, and further gas removal is dominated by star formation rather than outflows. Outflows in the center of starbursting disks, such as observed here, may therefore act to reduce the impacts of other effects that drive up the gas velocity dispersion. Theoretical work that incorporates outflows into dynamical equilibrium models of star formation may be necessary to explain high Σ_{SFR} disk galaxies.

We note that this is heuristically similar to a scenario in which feedback can be overcome on short timescales by very efficient star formation (Torrey et al. 2017). Orr et al. (2019) and Rathjen et al. (2021) made similar analyses of simulation data, at lower Σ_{mol} . The difference between IRAS08 and the conclusions in Torrey et al. (2017), however, is that in Torrey et al. (2017) this phenomenon only occurs over the very central nuclei of a galaxy, whereas in IRAS08 it extends beyond the half-light radius of the starlight. F22 reported short freefall times, ~ 1 –5 Myr in a very large fraction of the galaxy, and high star formation efficiencies per freefall time. Taken together, the observations of F22 and the outflow observations here are likewise conceptually consistent with the picture in which departures from dynamical equilibrium are regulated by strong winds.

We note that there are many similarities between IRAS08 and $z \sim 1$ –2 galaxies, including the higher gas fraction, high molecular gas velocity dispersion, and location in the $\Sigma_{\text{SFR}}-\Sigma_{\text{mol}}$ diagram (for a full comparison see F22). Our results may therefore indicate that the low molecular gas depletion times observed in galaxies at $z \sim 2$ (e.g., Tacconi et al. 2018; Herrera-Camus et al. 2019) may be due more to outflows depleting the local area of the disk, rather than conversion of gas into stars. What we do not currently know is which relationship is more important, that of $\dot{\Sigma}_{\text{out}} - \Sigma_{\text{SFR}}$ or

the relationship between outflow efficiency and star formation efficiency. For example, both Genzel et al. (2011) and Molina et al. (2019) found galaxies with high Σ_{mol} and Σ_{SFR} at sub-galactic resolution, but they have disk-like depletion times. Observations of outflows in systems like this would be informative.

Our work has shown the diagnostic power of comparing the properties of outflows to both Σ_{SFR} and Σ_{mol} in resolved observations. Tracking three of the parameters responsible for regulating star formation in galaxy disks in resolved observations enables us to make unique comparisons to theory. Yet we have examined only one galaxy. To repeat this on multiple targets, however, requires a substantial investment in observing time. Outflows are more easily detected on high-efficiency spectrographs on 8–10 m class telescopes (such as Keck/KCWI and VLT/MUSE). This then must be combined with data from millimeter-wave interferometers, such as the Atacama Large Millimeter/submillimeter Array (ALMA), SMA, and NOEMA. Finally, observations of the ratio of $\dot{M}_{\text{out}}(\text{ions})$ -to- $\dot{M}_{\text{out}}(\text{molecules})$ vary significantly on the handful of targets that have been measured (Fluetsch et al. 2019; Herrera-Camus et al. 2020). Combining resolved observations from optical and millimeter-wave instruments, we would ideally have much better constraints on the phase distribution of outflows. Deep ALMA observations of molecular gas outflows targeting galaxies with known ionized gas outflows would be very informative, as ionized gas outflows are much easier to observe, especially in more distant galaxies. We expect future work using DUVET galaxies to address these concerns.

We are grateful to Viraj Pandya for discussing and sharing FIRE-2 simulation results, and to Matt Orr for helpful discussion. Parts of this research were supported by the Australian Research Council Centre of Excellence for All Sky Astrophysics in 3 Dimensions (ASTRO 3D), through project number CE170100013. D.B.F. acknowledges support from Australian Research Council (ARC) Future Fellowship FT170100376 and ARC Discovery Program grant DP130101460. A.D.B. acknowledges support from NSF-AST2108140. A.J.C. acknowledges funding from the “First-Galaxies” Advanced Grant from the European Research Council (ERC) under the European Union’s Horizon 2020 research and innovation program (grant agreement No. 789056). R.H.-C. thanks the Max Planck Society for support under the Partner Group project “The Baryon Cycle in Galaxies” between the Max Planck for Extraterrestrial Physics and the Universidad de Concepción. R.H.-C. also acknowledges financial support from Millenium Nucleus NCN19058 (TITANs) and support by the ANID BASAL projects ACE210002 and FB210003. D.O. is a recipient of an Australian Research Council Future Fellowship (FT190100083) funded by the Australian Government. R.R. V. and K.S. acknowledge funding support from National Science Foundation Award No. 1816462.

This work is based on observations carried out under project No. W17CB with the IRAM NOEMA Interferometer. IRAM is supported by INSU/CNRS (France), MPG (Germany), and IGN (Spain).

Some of the data presented herein were obtained at the W. M. Keck Observatory, which is operated as a scientific partnership among the California Institute of Technology, the

University of California, and the National Aeronautics and Space Administration. The Observatory was made possible by the generous financial support of the W. M. Keck Foundation. Observations were supported by the Swinburne Keck program 2018A_W185. The authors wish to recognize and acknowledge the very significant cultural role and reverence that the summit of Mauna Kea has always had within the indigenous Hawaiian community. We are most fortunate to have the opportunity to conduct observations from this mountain.

Facilities: Keck:II (KCWI), IRAM:NOEMA

Software: koffee (Reichardt Chu et al. 2022, <https://github.com/bronreichardtchu/koffee/tree/PaperI-code>), astropy (Astropy Collaboration et al. 2013; Price-Whelan 2018)

ORCID iDs

Bronwyn Reichardt Chu <https://orcid.org/0000-0002-7187-8561>
 Deanne B. Fisher <https://orcid.org/0000-0003-0645-5260>
 Alberto D. Bolatto <https://orcid.org/0000-0002-5480-5686>
 John Chisholm <https://orcid.org/0000-0002-0302-2577>
 Drummond Fielding <https://orcid.org/0000-0003-3806-8548>
 Danielle Berg <https://orcid.org/0000-0002-4153-053X>
 Alex J. Cameron <https://orcid.org/0000-0002-0450-7306>
 Karl Glazebrook <https://orcid.org/0000-0002-3254-9044>
 Rodrigo Herrera-Camus <https://orcid.org/0000-0002-2775-0595>
 Glenn G. Kacprzak <https://orcid.org/0000-0003-1362-9302>
 Laura Lenkić <https://orcid.org/0000-0003-4023-8657>
 Daniel K. McPherson <https://orcid.org/0000-0001-9345-7234>
 Nikole M. Nielsen <https://orcid.org/0000-0003-2377-8352>
 Danail Obreschkow <https://orcid.org/0000-0002-1527-0762>
 Ryan J. Rickards Vaught <https://orcid.org/0000-0001-9719-4080>
 Karin Sandstrom <https://orcid.org/0000-0002-4378-8534>

References

Ambachew, L., Fisher, D. B., Glazebrook, K., et al. 2022, *MNRAS*, **512**, 3079
 Arribas, S., Colina, L., Bellocchi, E., Maiolino, R., & Villar-Martín, M. 2014, *A&A*, **568**, A14
 Astropy Collaboration, Robitaille, T. P., Tollerud, E. J., et al. 2013, *A&A*, **558**, A33
 Avery, C. R., Wuyts, S., Förster Schreiber, N. M., et al. 2021, *MNRAS*,
 Barrera-Ballesteros, J. K., Sánchez, S. F., Heckman, T., et al. 2021, *MNRAS*, **503**, 3643
 Bigiel, F., Leroy, A., Walter, F., et al. 2008, *AJ*, **136**, 2846
 Bolatto, A. D., Leroy, A. K., Levy, R. C., et al. 2021, *ApJ*, **923**, 83
 Bolatto, A. D., Warren, S. R., Leroy, A. K., et al. 2013a, *Natur*, **499**, 450
 Bolatto, A. D., Wolfire, M., & Leroy, A. K. 2013b, *ARA&A*, **51**, 207
 Boquien, M., Burgarella, D., Roehlly, Y., et al. 2019, *A&A*, **622**, A103
 Calzetti, D. 2001, *PASP*, **113**, 1449
 Calzetti, D., Armus, L., Bohlin, R. C., et al. 2000, *ApJ*, **533**, 682
 Cameron, A. J., Fisher, D. B., McPherson, D., et al. 2021, *ApJL*, **918**, L16
 Cappellari, M. 2017, *MNRAS*, **466**, 798
 Chen, Y.-M., Tremonti, C. A., Heckman, T. M., et al. 2010, *AJ*, **140**, 445
 Chisholm, J., Tremonti, C. A., Leitherer, C., et al. 2015, *ApJ*, **811**, 149
 Chisholm, J., Tremonti, C. A., Leitherer, C., & Chen, Y. 2017, *MNRAS*, **469**, 4831
 Chisholm, J., Tremonti, C. A., Leitherer, C., Chen, Y., & Wofford, A. 2016, *MNRAS*, **457**, 3133
 Conroy, C., Gunn, J. E., & White, M. 2009, *ApJ*, **699**, 486
 Davies, R. L., Schreiber, N. F., Übler, H., et al. 2019, *ApJ*, **873**, 122
 Dekel, A., Sari, R., & Ceverino, D. 2009, *ApJ*, **703**, 785
 Faucher-Giguère, C.-A., Quataert, E., & Hopkins, P. F. 2013, *MNRAS*, **433**, 1970

Fielding, D., Quataert, E., & Martizzi, D. 2018, *MNRAS*, **481**, 3325

Fielding, D., Quataert, E., Martizzi, D., & Faucher-Giguère, C.-A. 2017, *MNRAS*, **470**, L39

Fielding, D. B., & Bryan, G. L. 2022, *ApJ*, **924**, 82

Fisher, D. B., Bolatto, A. D., Glazebrook, K., et al. 2022, *ApJ*, **928**, 169

Fisher, D. B., Bolatto, A. D., White, H., et al. 2019, *ApJ*, **870**, 46

Fluetsch, A., Maiolino, R., Carniani, S., et al. 2019, *MNRAS*, **483**, 4586

Fluetsch, A., Maiolino, R., Carniani, S., et al. 2021, *MNRAS*, **505**, 5753

Förster Schreiber, N., Übler, H., Davies, R., et al. 2019, *ApJ*, **875**, 21

Gentry, E. S., Madau, P., & Krumholz, M. R. 2020, *MNRAS*, **492**, 1243

Genzel, R., Newman, S., Jones, T., et al. 2011, *ApJ*, **733**, 101

Girard, M., Fisher, D. B., Bolatto, A. D., et al. 2021, *ApJ*, **909**, 12

Grudić, M. Y., Hopkins, P. F., Faucher-Giguère, C.-A., et al. 2018, *MNRAS*, **475**, 3511

Hao, C.-N., Kennicutt, R. C., Johnson, B. D., et al. 2011, *ApJ*, **741**, 124

Hayward, C. C., & Hopkins, P. F. 2017, *MNRAS*, **465**, 1682

Heckman, T. M., Alexandroff, R. M., Borthakur, S., Overzier, R., & Leitherer, C. 2015, *ApJ*, **809**, 147

Heckman, T. M., Lehnert, M. D., Strickland, D. K., & Armus, L. 2000, *ApJS*, **129**, 493

Herrera-Camus, R., Janssen, A., Sturm, E., et al. 2020, *A&A*, **635**, A47

Herrera-Camus, R., Tacconi, L., Genzel, R., et al. 2019, *ApJ*, **871**, 37

Hinshaw, G., Larson, D., Komatsu, E., et al. 2013, *ApJS*, **208**, 19

Hopkins, P. F., Quataert, E., & Murray, N. 2012, *MNRAS*, **421**, 3522

Kennicutt, R. C. J. 1989, *ApJ*, **344**, 685

Kennicutt, R. C., Jr, & Evans, N. J. 2012, *ARA&A*, **50**, 531

Kewley, L. J., Nicholls, D. C., & Sutherland, R. S. 2019, *ARA&A*, **57**, 511

Kim, C.-G., & Ostriker, E. C. 2017, *ApJ*, **846**, 133

Kim, C.-G., Ostriker, E. C., & Kim, W.-T. 2013, *ApJ*, **776**, 1

Kim, C.-G., Ostriker, E. C., Somerville, R. S., et al. 2020, *ApJ*, **900**, 61

Kim, D. C., Sanders, D. B., Veilleux, S., Mazzarella, J. M., & Soifer, B. T. 1995, *ApJS*, **98**, 129

Kroupa, P., & Weidner, C. 2003, *ApJ*, **598**, 1076

Krumholz, M. R., Burkhardt, B., Forbes, J. C., & Crocker, R. M. 2018, *MNRAS*, **477**, 2716

Leitherer, C., Chandar, R., Tremonti, C. A., Wofford, A., & Schaerer, D. 2013, *ApJ*, **772**, 120

Leitherer, C., Li, I. H., Calzetti, D., & Heckman, T. M. 2002, *ApJS*, **140**, 303

Leroy, A. K., Bolatto, A. D., Ostriker, E. C., et al. 2015a, *ApJ*, **801**, 25

Leroy, A. K., Walter, F., Martini, P., et al. 2015b, *ApJ*, **814**, 83

Leroy, A. K., Walter, F., Sandstrom, K., et al. 2013, *AJ*, **146**, 19

Li, M., Bryan, G. L., & Ostriker, J. P. 2017, *ApJ*, **841**, 101

López-Sánchez, Á. R., Esteban, C., & García-Rojas, J. 2006, *A&A*, **449**, 997

Luridiana, V., Morisset, C., & Shaw, R. A. 2015, *A&A*, **573**, A42

Molina, J., Ibar, E., Smail, I., et al. 2019, *MNRAS*, **487**, 4856

Morrissey, P., Matuszewski, M., Martin, D. C., et al. 2018, *ApJ*, **864**, 93

Muratov, A. L., Kereš, D., Faucher-Giguère, C.-A., et al. 2015, *MNRAS*, **454**, 2691

Nelson, D., Pillepich, A., Springel, V., et al. 2019, *MNRAS*, **490**, 3234

Newman, S. F., Genzel, R., Förster-Schreiber, N. M., et al. 2012, *ApJ*, **761**, 43

Oppenheimer, B. D., Davies, J. J., Crain, R. A., et al. 2020, *MNRAS*, **491**, 2939

Orr, M. E., Fielding, D. B., Hayward, C. C., & Burkhardt, B. 2022a, *ApJL*, **924**, L28

Orr, M. E., Fielding, D. B., Hayward, C. C., & Burkhardt, B. 2022b, *ApJ*, **932**, 88

Orr, M. E., Hayward, C. C., & Hopkins, P. F. 2019, *MNRAS*, **486**, 4724

Osterbrock, D. E., & Ferland, G. J. 2006, *Astrophysics of Gaseous Nebulae and Active Galactic Nuclei* (2nd ed.; Sausalito, CA: University Science Books)

Ostriker, E. C., & Kim, C.-G. 2022, *ApJ*, **936**, 137

Ostriker, E. C., McKee, C. F., & Leroy, A. K. 2010, *ApJ*, **721**, 975

Otf-Floranes, H., Mas-Hesse, J. M., Jiménez-Bailón, E., et al. 2014, *A&A*, **566**, A38

Price-Whelan, A. M., Sipőcz, B. M., Rix, H.-W., et al. 2018, *AJ*, **156**, 123

Pandya, V., Fielding, D. B., Anglés-Alcázar, D., et al. 2021, *MNRAS*, **508**, 2979

Rathjen, T.-E., Naab, T., Girichidis, P., et al. 2021, *MNRAS*, **504**, 1039

Reichardt Chu, B., Fisher, D. B., Nielsen, N. M., et al. 2022, *MNRAS*, **511**, 5782

Roberts-Borsani, G. W., Saintonge, A., Masters, K. L., & Stark, D. V. 2020, *MNRAS*, **493**, 3081

Rodríguez del Pino, B., Arribas, S., Piqueras López, J., Villar-Martín, M., & Colina, L. 2019, *MNRAS*, **486**, 344

Romeo, A. B., Burkert, A., & Agertz, O. 2010, *MNRAS*, **407**, 1223

Rubin, K. H. R., Prochaska, J. X., Koo, D. C., et al. 2014, *ApJ*, **794**, 156

Rupke, D. S., Veilleux, S., & Sanders, D. B. 2005, *ApJS*, **160**, 115

Salak, D., Nakai, N., Sorai, K., & Miyamoto, Y. 2020, *ApJ*, **901**, 151

Shopbell, P. L., & Bland-Hawthorn, J. 1998, *ApJ*, **493**, 129

Somerville, R. S., & Davé, R. 2015, *ARA&A*, **53**, 51

Stanway, E. R., & Eldridge, J. J. 2018, *MNRAS*, **479**, 75

Steidel, C. C., Erb, D. K., Shapley, A. E., et al. 2010, *ApJ*, **717**, 289

Sun, J., Leroy, A. K., Ostriker, E. C., et al. 2020, *ApJ*, **892**, 148

Tacconi, L. J., Genzel, R., Saintonge, A., et al. 2018, *ApJ*, **853**, 179

Torrey, P., Hopkins, P. F., Faucher-Giguère, C.-A., et al. 2017, *MNRAS*, **467**, 2301

Veilleux, S., Cecil, G., & Bland-Hawthorn, J. 2005, *ARA&A*, **43**, 769

Veilleux, S., Maiolino, R., Bolatto, A. D., & Aalto, S. 2020, *A&ARv*, **28**, 2

Veilleux, S., & Rupke, D. S. 2002, *ApJL*, **565**, L63

Wilson, C. D., Elmegreen, B. G., Bemis, A., & Brunetti, N. 2019, *ApJ*, **882**, 5